Temporal and Spatial Heterogeneity of Host Response to SARS-CoV-2 Pulmonary Infection

Niyati Desai[1,*], Azfar Neyaz[1,*], Annamaria Szabolcs[1,*], Angela R. Shih[2,*], Jonathan H. Chen[1,2], Vishal Thapar[1], Linda T. Nieman[1], Alexander Solovyov[5], Arnav Mehta[1,4], David J. Lieb [4], Anupriya S. Kulkarni[1], Christopher Jaicks[1], Christopher J. Pinto[1], Dejan Juric [1], Ivan Chebib [2], Robert B. Colvin[2], Arthur Y. Kim[3], Robert Monroe[6], Sarah E Warren[7], Patrick Danaher[7], Jason W Reeves[7], Jingjing Gong[7], Erroll H Rueckert[7], Benjamin D. Greenbaum[5], Nir Hacohen[1,3,4], Stephen M. Lagana[8], Miguel N. Rivera[1,2,4], Lynette M. Sholl[9], James R. Stone[2,#], David T. Ting[1,3,#], Vikram Deshpande[1,2,#]

[1] Massachusetts General Hospital Cancer Center, Departments of [2]Pathology and [3]Medicine, Boston, MA 02114, USA
[4] The Broad Institute, Cambridge, MA 02142, USA
[5] Memorial Sloan Kettering Cancer Center, New York, NY 10065, USA
[6] Advanced Cell Diagnostics, a Bio-Techne Brand, Newark, CA 94560, USA
[7] NanoString Inc., Seattle, WA 98109, USA
[8] Columbia University Irving Medical Center, Department of Pathology and Cell Biology, New York, NY 10032, USA
[9] Brigham and Woman's Hospital, Department of Pathology, Boston, MA 02115

* Equal contribution
# Equal contribution and address correspondence to

James R. Stone (jrstone@mgh.harvard.edu)
Massachusetts General Hospital
Department of Pathology
149 13th Street, Room 7368
Charlestown, MA, 02129
Phone 617-726-8303, Fax 617-643-3566

David T. Ting (dting1@mgh.harvard.edu)
Massachusetts General Hospital Cancer Center
149 13th Street, Room 618B
Charlestown, Massachusetts 02129
Tel: 617-240-9402   Fax: 617 724-3676

Vikram Deshpande (vdeshpande@mgh.harvard.edu)
Massachusetts General Hospital
Department of Pathology
55 Fruit St., Warren 2
Boston, MA 02114-2696
Tel: 617-726-7741   Fax: 617-726-7474

1

ABSTRACT (100 words)

The relationship of SARS-CoV-2 lung infection and severity of pulmonary disease is not fully understood. We analyzed autopsy specimens from 24 patients who succumbed to SARS-CoV-2 infection using a combination of different RNA and protein analytical platforms to characterize inter- and intra- patient heterogeneity of pulmonary virus infection. There was a spectrum of high and low virus cases that was associated with duration of disease and activation of interferon pathway genes. Using a digital spatial profiling platform, the virus corresponded to distinct spatial expression of interferon response genes and immune checkpoint genes demonstrating the intra-pulmonary heterogeneity of SARS-CoV-2 infection.

INTRODUCTION

The coronavirus disease 2019 (COVID-19) pandemic is caused by the betacoronavirus severe acute respiratory syndrome coronavirus 2 (SARS-CoV-2)[1]. Although there has been significant progress in understanding the factors involved with SARS-CoV-2 cellular infectivity, the relationship of SARS-CoV-2 lung infection and severity of pulmonary disease manifestations is not fully understood. Immune responses to viral infection have evolved to clear the pathogen, and differences in these responses amongst patients is likely to affect clinical outcomes. Autopsy series have revealed that the predominant pattern of lung injury in COVID-19 patients is diffuse alveolar damage, characterized by hyaline membrane formation and in most cases, a presumed healing phase of this lesion[2]. However, these studies are limited in their ability to elucidate the complex immune response in SARS-CoV-2 pulmonary infection. An initial brief report of single cell RNA-seq analysis of bronchoalveolar lavage fluid from 9 patients noted an abundance of inflammatory monocyte-derived macrophages, lower CD8+ T cell infiltration, and high cytokine levels (IL-8, IL-6 and IL-1β) in patients with severe COVID-19[3]. This suggested that macrophage driven responses and a "cytokine storm" were potentially preventing adequate T cell response to SARS-CoV-2 in patients with severe disease. Another study of 3 patients that focused on the peripheral blood response to SARS-CoV-2 found elevated IL-1 pathway cytokines and subsequent decrease in peripheral T cells, potentially linking intrapulmonary immune response with systemic changes[4].

There have been a number of studies that have examined the blood based immune response to SARS-CoV-2 infection[5-7]. Tissue based examination has the potential to provide a more accurate assessment of SARS-CoV-2 related immune signatures, particularly if the immune cells are restricted to the affected organs. The ability to visualize SARS-CoV-2 at a tissue level provides unique information on the cell types infected by the virus and the spatial relationship of infected cells with immune and non-immune cells in the microenvironment. This provides a

3

strategy to elucidate the roles of direct viral cytopathic effect and cellular injury from aberrant immune reaction, both within the lung and at extra-pulmonary sites[8,9]. Herein, we examined autopsy material from 24 COVID-19 patients collected at two institutions. The results demonstrate heterogeneous levels of SARS-CoV-2 RNA which correlate with duration of disease and show a range of host immune response patterns as well as significant spatial heterogeneity of both viral load and immune response.

RESULTS

Detection of SARS-CoV-2 in Human Lung Autopsy Tissue Associated with Duration of Disease

A total of 20 patients at the Massachusetts General Hospital and 4 patients from Columbia University Irving Medical Center (NYC) who succumbed from SARS-CoV-2 infection underwent autopsy upon consent for clinical care. All patients were confirmed for SARS-CoV-2 infection through qRT-PCR assays performed on nasopharyngeal swab specimens. Clinical summaries of the 24 patients are listed in Supplementary Table 1. The mean age of this cohort was 62.5 years (range 32-89) with 14 males and 10 females. A total of 17 patients had medication records available with 5/17 patients on immunosuppressive medications, including 3 patients on corticosteroids. Most patients received hydroxychloroquine (13/17 = 76%), while none received remdesivir.

Cases were evaluated with RNA *in situ* hybridization (RNA-ISH) using a SARS-CoV-2 RNA specific probe targeting the S gene applied to multiple at least 2 different lobes of the lung and selected extrapulmonary organs. RNA-ISH positive cases noted intracellular staining detectable with a predominance in pneumocytes (Fig. 1a). Robust extracellular staining in hyaline membranes was detectable in 11 of 23 cases (Fig. 1a). One sample (Case A) failed by RNA-

ISH due to sample quality. Preservation of RNA quality was confirmed by GAPDH RNA-ISH. A similar pattern of reactivity was noted on an immunohistochemical stain for the SARS-CoV nucleocapsid protein (Supplementary Fig. 1).

Based on a quantitative assessment of the RNA-ISH (high viral cases defined as ratio of area of viral infected lung to total lung area $\geq$ 2%), 11 cases were classified as high viral RNA (Cases 1, 5, 7, 8, 9, 11, 15, 16, 18, C, D) while 12 cases were characterized as low viral RNA (Cases 2, 3, 4, 6, 10, 12, 13, 14, 17, 19, 20, B). High viral RNA correlated with extracellular viral RNA in a hyaline membrane pattern (Chi square p=0.001; Fig. 1b).

The histological analysis of the tissue sections used for viral RNA-ISH revealed a mixed picture with 5 cases showing only acute diffuse alveolar damage pattern of injury; in 9 patients the acute injury was accompanied by interstitial and/or airspace organization. Two cases lacked acute injury, instead showing only organizing-pattern injury. Low viral RNA correlated with evidence of interstitial/airway organization (p=0.049). Of note, the two patients with the purely organizing pattern of injury showed extremely low viral RNA (0% and 0.01%). Cases with low viral RNA also showed higher numbers of Napsin A positive cells (p=0.02) and trend towards higher keratin positive cells (p=0.08), supporting the repopulation of pneumocytes/bronchial epithelial cells. Collectively, early pattern of lung injury (exudative diffuse alveolar damage) correlated with high viral RNA while the presence of organization and intact pneumocytes correlated with low viral RNA.
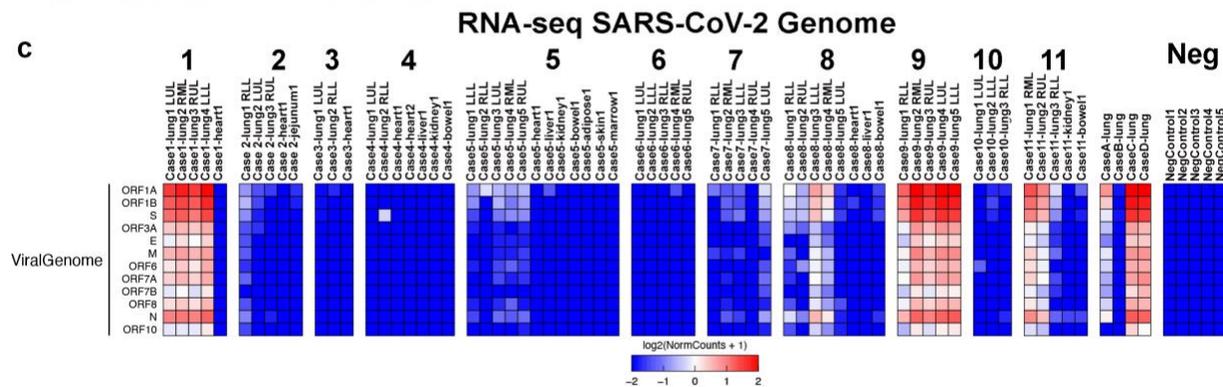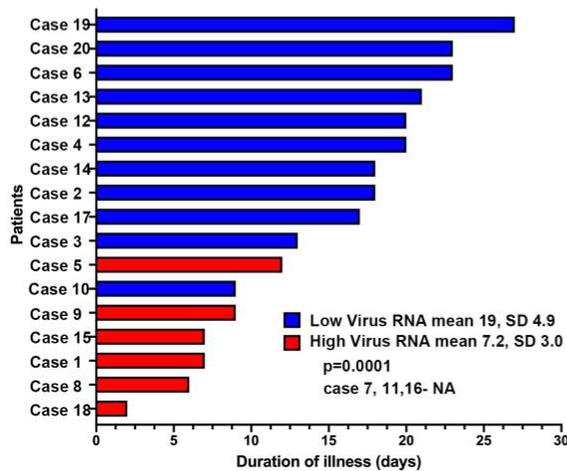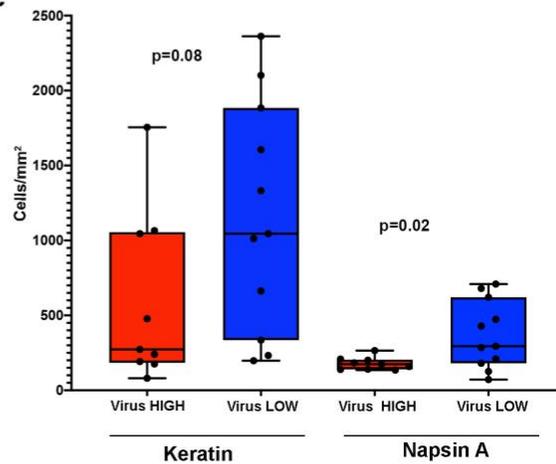
Figure 1
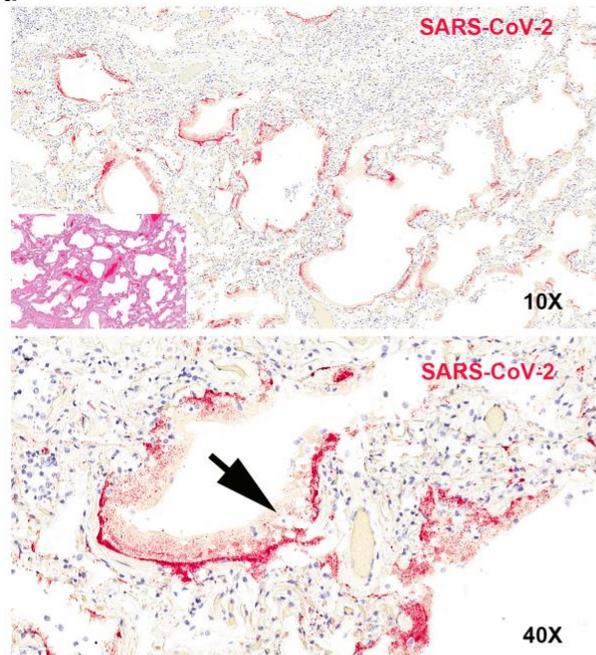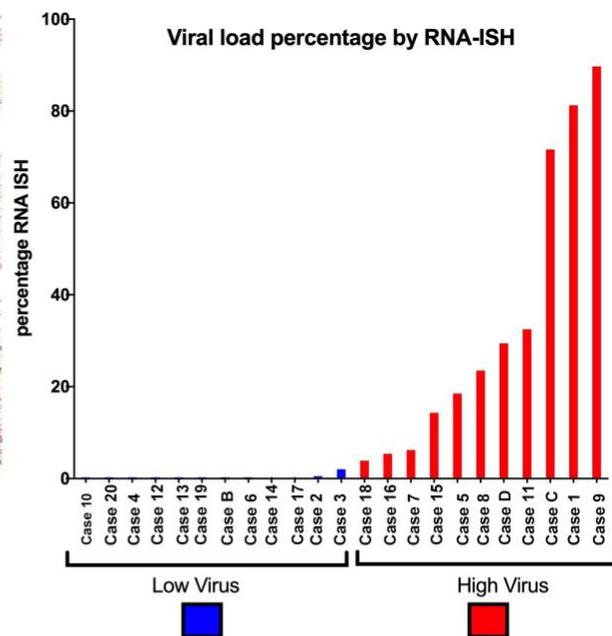
Fig. 1 Detection of SARS-CoV-2 in Human Autopsy Samples.
a, Paraffin embedded sections from the lung of Case1 show abundant SARS-CoV-2 extracellular RNA-ISH signal (red) predominantly localization to the hyaline membranes (arrow). The inset shows the corresponding hematoxylin and eosin stained section shows histologic features of exudative diffuse alveolar damage with prominent hyaline membranes.
b, Percentage of viral load in the lung as determined by a quantitative analysis of SARS-CoV-2 RNA-ISH.
c, Expression heatmap of RNA-seq aligned counts of genes in the SARS-CoV-2 genome Log2(RPM) from autopsy cases. Consistent with the quantitative analysis on the RNA-ISH platform, cases 9, 1, C, 11, D and case 8 showed the highest viral load. The non-pulmonary organs were virtually negative for virus, except two bowel tissues.
d, Swimmers plot highlighting difference in duration of illness between viral high and viral low cases.
e, Quantitative protein expression of keratin and Napsin A by immunohistochemistry performed on lung sections between viral high and low cases. Viral low cases showed higher number of keratin and Napsin A positive cells, both surrogate markers of pulmonary pneumocytes. Box-and-whisker plot, center line, median; box limits, upper and lower quartiles; whiskers, range. P-value two tailed t-test.

7

To validate the RNA-ISH data, we performed molecular confirmation through quantitative RT-PCR (qRT-PCR)(Supplementary Fig. 2) and Total RNA-sequencing (RNA-seq)(Fig. 1c) for Cases 1-11, Cases A-D, and 5 non-COVID-19 autopsy lung specimens (Negative Control). There was concordance of orthogonal techniques of viral detection, although as expected, qRT-PCR had the highest sensitivity of detecting SARS-CoV-2 in tissues (Supplementary Data1, Supplementary Table 3). RNA-seq also identified negative sense viral reads in most specimens with detectable virus indicating active viral replication in the lung (Supplementary Table 6). Interestingly, antisense viral transcripts averaged 12.4% of total viral transcripts across all samples with detectable viral transcripts. The sense percentage was higher in the viral high cases, although this difference was not statically significant (mean 91.1% vs 81.6%; p=0.24).

Other organs examined in these cases including the heart, liver, jejunum, bowel, bone marrow, adipose tissue, skin and kidney were negative for detectable SARS-CoV-2 by RNA-ISH (Supplementary Data 1). Total RNA-seq detected viral RNA in two bowel samples (Cases 8 and 11). All other extrapulmonary samples were negative for SARS-CoV-2 by total RNA-seq. The absence of detectable virus by RNA-ISH suggests that viral RNA detected in non-pulmonary organs may represent viral RNA in blood, or that viral load is beneath the limit of detection by ISH.

We then evaluated if RNA-ISH viral load were associated with clinical parameters in our cases (Supplementary Table 1). Patients classified as high viral RNA showed a shorter duration of disease (mean 7.2 days, SD 3.02) than patients with low viral load (mean 19 days, SD 4.9) (Fig. 1d; t-test p=0.0001). Additionally, patients classified as high viral RNA load had significantly fewer days in the hospital (mean 3.6 days, SD 2.2) than patients with low viral load (mean 14 days, SD 7.9) (t-test p=0.003). These differences could be because of a higher proportion of patients not receiving intubation and mechanical ventilation in the high viral RNA cases (4/9 vs

8

10/11, Fisher Exact p = 0.049). Although the limited number of cases precluded correlation with parameters associated with a cytokine syndrome,[10,11] all parameters, except for absolute lymphocyte counts, showed higher numbers in low viral cases, although none of these were statistically significant (Supplementary Table 2). There were no correlations between viral load and age, gender or immunosuppression medication. Collectively, the data suggest a predictable pattern of viral infection manifested histologically by prominent diffuse alveolar damage with robust reactivity by RNA-ISH in the early phase and a shift towards organizing fibrosis with more sparse reactivity by RNA-ISH in the later phase.

**Significant Innate Immune Response in High SARS-CoV-2 Infected Lungs**

We next investigated gene expression patterns in separate lobes of the lung (left lower lobe - LLL, left upper lobe - LUL, right lower lobe - RLL, right middle lobe - RML, right upper lobe - RUL) from SARS-CoV-2 cases using total RNA-seq. Unsupervised hierarchical clustering of samples for the 500 most variant genes demonstrated a separation of high viral RNA samples from low viral RNA samples (Fig. 2a). Notably, there was separate clustering of high viral cases (Cases 1, 8, 9, 11, C, D) and low viral cases (Cases 3, 4, 6, 10, B), but interestingly, there was a separate cluster containing lung specimens from both high and low viral cases (Cases 2, 3, 5). Cases 2 and 5 both had intermediate levels of virus when compared to other cases. In addition, the left upper lobe in Case 7 was notable for having very high viral levels unlike the other 4 lobes that had low virus. Gene set enrichment analysis for genes that were different between the three clusters (colored boxed Fig. 2a) was done to understand the host response differences between these lung samples by viral load strata (Supplemental Data 2). The virus high cluster had high expression of interferon stimulated genes (ISGs) including *IRF1*, *IFI44L*, *IFIT3*, and antiviral genes (*OAS3*, *ADAR*) with significant enrichment of interferon (IFN) pathway gene sets including HALLMARK_INTERFERON_GAMMA_RESPONSE (FDR = 1.04E-24) and HALLMARK_INTERFERON_ALPHA_RESPONSE (FDR = 1.43 E-21). High virus samples also

9

had enrichment of HALLMARK_EPITHELIAL_MESENCHYMAL_TRANSITION (FDR = 3.13E-12) consistent with wound healing in these SARS-CoV-2 infected lungs. The mixed virus cluster noted high expression of multiple collagen genes (*COL1A1*, *COL1A2*, *COL3A1*, *COL4A1*, *COL4A2*, *COL5A1*, *COL6A1*, *COL6A2*, *COL6A3*) along with other genes enriched in HALLMARK_EPITHELIAL_MESENCHYMAL_TRANSITION (FDR = 4.60 E-25) and HALLMARK_MYOGENESIS (FDR = 5.53 E-09), alluding to continued wound healing and early fibrosis. Both high and mixed virus clusters had genes elevated in HALLMARK_COAGULATION (High virus cluster FDR = 2.19 E-10; Mixed virus cluster FDR = 1.46 E-06) with notable increased expression of *PECAM1* (CD31) and *VWF*, two well-known markers for endothelial cells in this gene set, indicating potential implications on pulmonary vasculature and coagulation. Low virus samples had notable elevated surfactant genes (*SFTPB*, *SFTPC*, *SFTPA1*, *SFTPA2*), mucins (*MUC2*, *MUC3A*, *MUC4*, *MUC5AC*, *MUC16*), and keratins (*KRT4*, *KRT5*, *KRT6A*, *KRT13*). These genes are enriched in epithelial cells and would suggest higher proportion of airway and alveolar lining cells, as opposed to inflammatory cells, in low viral lung specimens. Together, these findings indicate there is a spectrum of viral load not only between patients, but also within the same patient that correlates with different transcriptional profiles of the host response.

We then analyzed RNA-seq data based on patient lung viral load and not individual samples as done with clustering. Using a cutoff of an average of 50 reads per million (RPM) of total viral gene expression across lung samples, we separated patients into high and low virus that was concordant with RNA-ISH results with the exception of Case 7, which again had one lung lobe (LUL) having high expression levels of virus (pink star) and 3 additional lobes (RLL, RML, LLL) that had detectable virus but below 50 RPM. Unbiased differential expression analysis (FDR < 0.01) identified 338 host genes that were higher in the high viral cases and 5710 genes higher in the low viral cases (Supplemental Data 3). The genes expressed higher in high viral cases

10

were enriched for IFN response (HALLMARK_INTERFERON_GAMMA_RESPONSE FDR =

2.66 E-81; HALLMARK_INTERFERON_ALPHA_RESPONSE (FDR = 1.40 E-75) with 60 IFN

gamma response genes (Fig. 2b). HALLMARK_EPITHELIAL_MESENCHYMAL_TRANSITION

(FDR = 3.90 E-14) and HALLMARK_COAGULATION (FDR = 2.54 E-08) were also enriched in

high versus low cases (Supplementary Fig. 3).

Figure 2
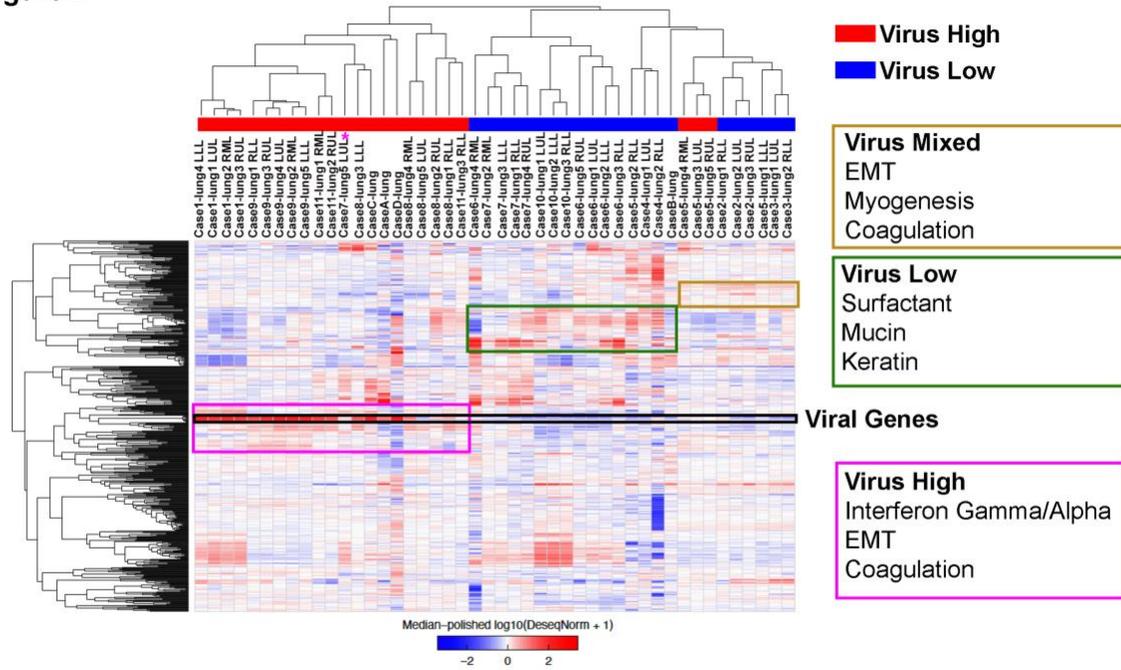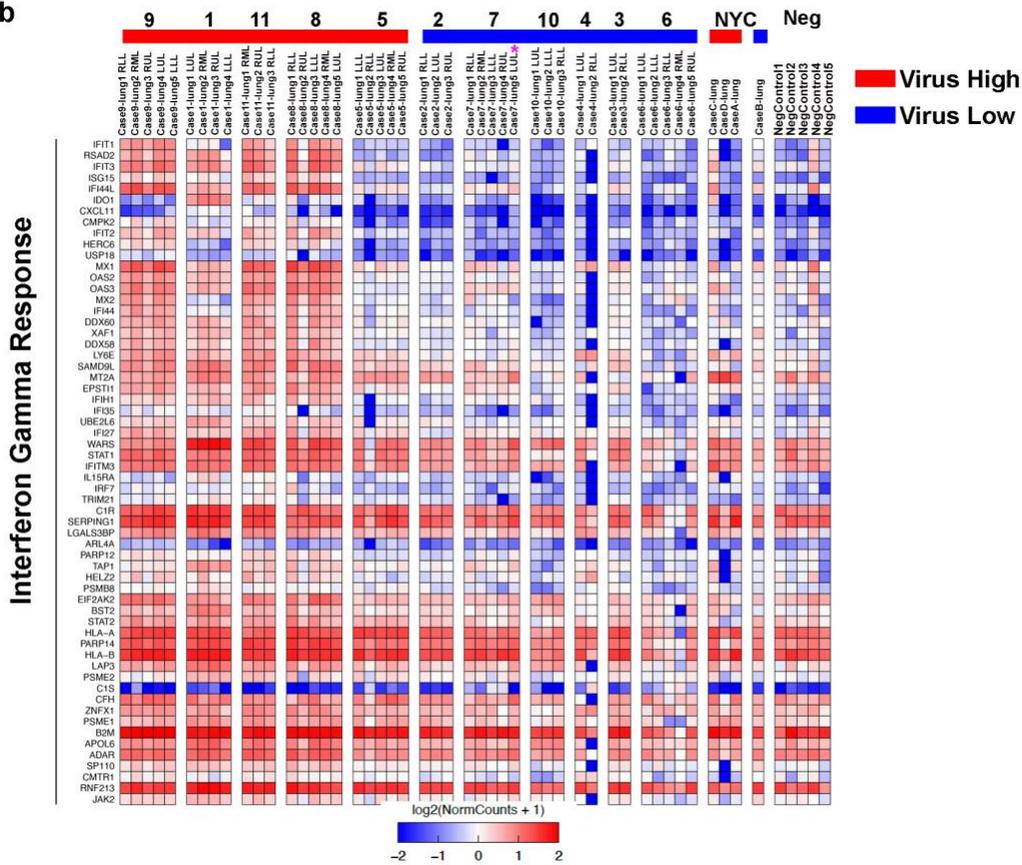
Figure 2: Interferon gamma response genes define high SARS-CoV-2 cases
**a,** Unsupervised hierarchical clustering of 500 most variant genes across lung specimens from SARS-CoV-2 infected patients separating into high, mixed, and low viral RNA cases.
b, Gene expression heatmap of interferon gamma response genes differentially expressed between high and low viral RNA cases. The high viral cases were enriched with higher interferon response genes.

13

We next looked at factors shown to be potentially involved in SARS-CoV-2 infectivity including *TMPRSS2*, *ACE2*, and CD147 (*BSG*)[12,13]. *CD147/BSG* had the highest mean expression (120.5 RPM) and *ACE2* the lowest (4.2 RPM) with frequent undetectable levels in COVID-19 lung samples (Fig. 3a). *TMPRSS2* had moderate expression in all lung samples (mean 27.2 RPM), and interestingly, was significantly lower in virus high compared to low samples (-1.72 Fold; FDR 0.0036). Recent single cell RNA-seq work in normal lungs has shown low expression of *ACE2* and higher expression of *TMPRSS2* in a subpopulation of pneumocytes, consistent with our findings[14]. This difference may reflect selective destruction of *TMPRSS2* positive pneumocytes in high relative to low viral infections and repopulation by pneumocytes. Analysis of immune cell and inflammatory markers[15] by RNA-seq showed a predominance of macrophage markers in all cases compared to other immune cells with markedly high expression of *CD163* (Fig. 3a and Supplementary Fig. 4). Analysis also showed markedly increased expression of multiple MHC Class I related genes (*HLA-A*, *HLA-B, HLA-C*, *B2M*, *TAP1*) in viral high versus low cases, which is consistent with high interferon activity.

We validated our immune cell RNA-seq analysis with IHC and quantification of immune cell types, which again showed very high numbers of CD163 positive cells in all samples (Fig. 3b and c). There was a non-significant trend toward higher CD163 (p=0.07), CD3 (p=0.06), and CD4 (p=0.14) in low viral cases. To determine if there were differences in the type of CD163 cells, we performed deconvolution of RNA-seq data (Fig. 3d and Supplementary Fig. 5), which showed lower cellular fraction of uncommitted (M0) macrophages (p = 0.01) in low viral cases and higher M1 polarized macrophages in high viral cases (p = 0.015). There was also a trend towards M2 polarization seen in low viral cases (p = 0.07).

14

Figure 3
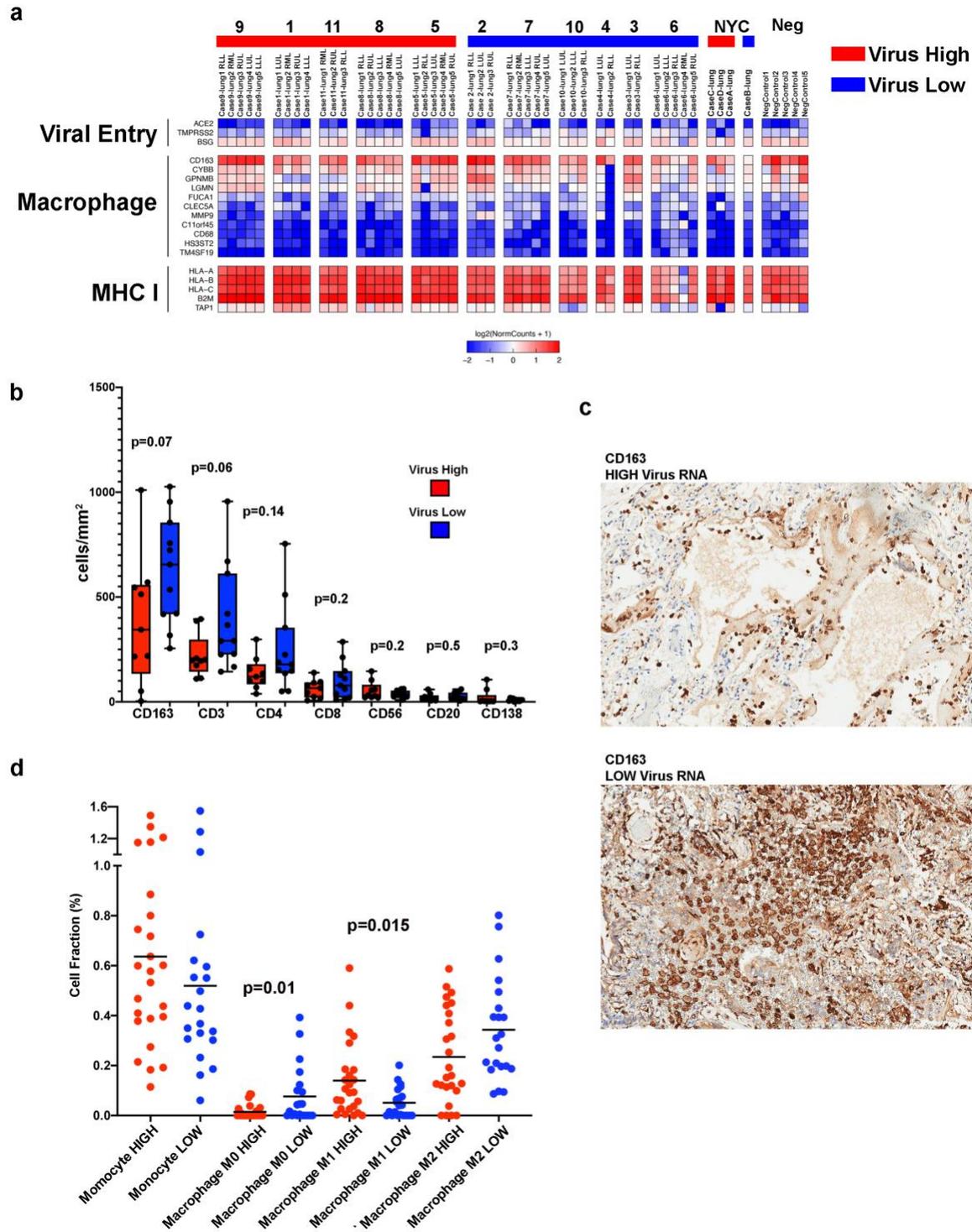
Fig. 3 Monocytes and Macrophages Dominate SARS-CoV-2 Lung Immune Response
a, Expression heatmap of genes involved with SARS-CoV-2 viral entry,
macrophage/monocytes, and MHC Class I.
b, Immunohistochemical quantitation of immune cell subsets in lung samples for CD163, CD3,
CD4, CD8, CD56, CD20, and CD138. Box-and-whisker plot, center line, median; box limits,
upper and lower quartiles; whiskers, range. P-value two tailed t-test.
c, Representative images of CD163 IHC staining in virus high and virus low case.
d, Cell fraction (%) of immune cell estimated in lung tissue obtained by deconvolution of bulk
RNA-seq data using CIBERSORTx. Bar = mean. P-value two tailed t-test.

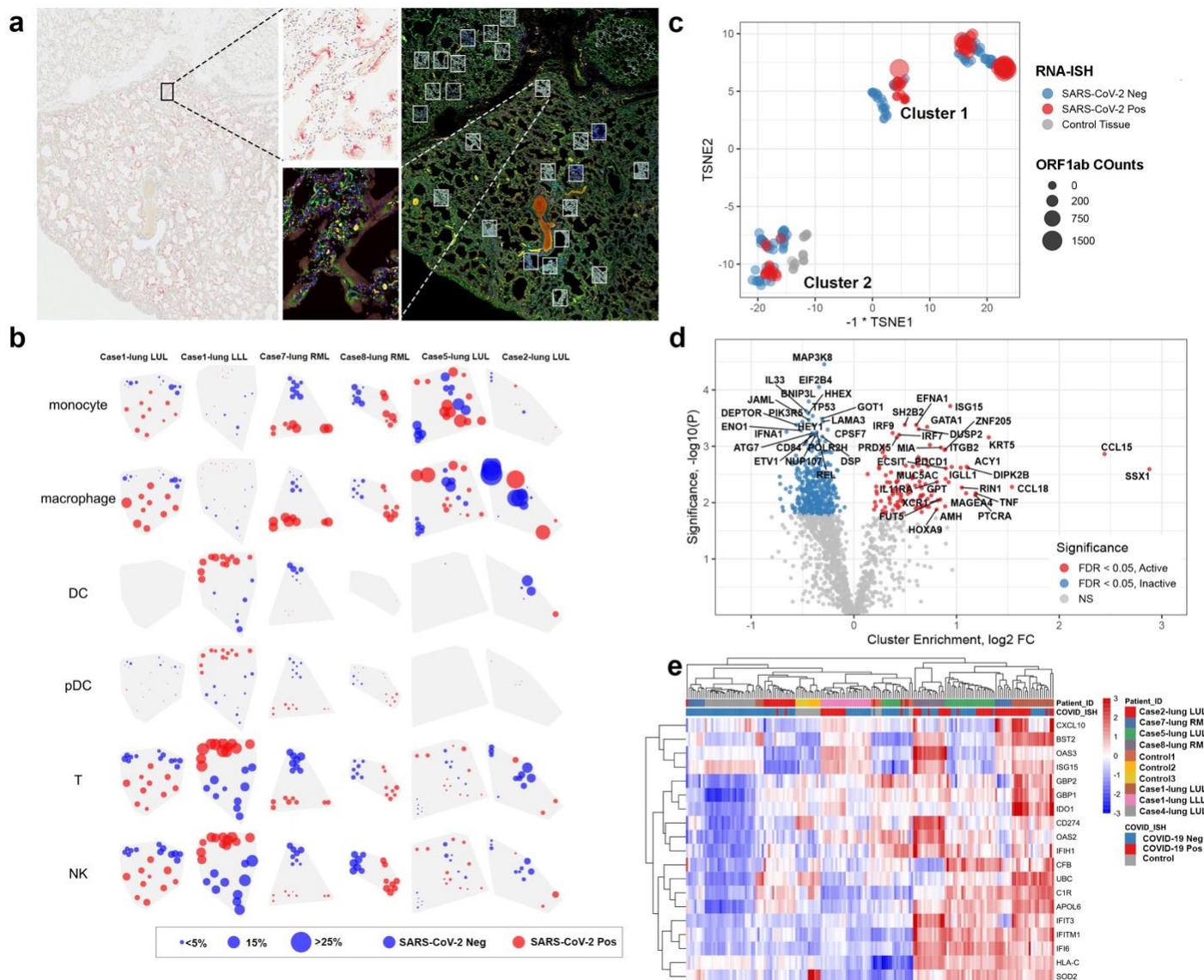**Intrapulmonary heterogeneity of immune response to SARS-CoV-2**

Given our observation that individual patients demonstrated anatomical heterogeneity with respect to histopathology and viral load, an in-depth assessment of the immune response within infected airspaces was undertaken. This was accomplished by the viral RNA directed sampling of paraffin embedded tissue sections using the GeoMxTM Digital Spatial Profiler (DSP)[16] in 6 lobes from 5 patients. Quantitative analysis of RNA and protein in discreet regions of interest (ROIs) was performed separately on SARS-CoV-2 viral positive and negative areas as identified by RNA-ISH (Fig. 4a). Deconvolution of immune subsets using RNA expression profiles of each ROI noted significant spatial heterogeneity of the immune response across cases (Fig. 4b). Macrophages were more abundant in areas with SARS-CoV-2 virus present (red circles) compared to non-viral areas (blue circles) in 4 of the 6 tissues with detectable virus. However, Case 2-lung LUL with very low virus had regions of high macrophage infiltrate without detectable virus. Interestingly, Case 1-lung LLL was very different from the other specimens with high dendritic cells (DC), T-cells, NK cells, and to a lesser extent plasmacytoid DCs (pDCs) in SARS-CoV-2 virus areas without monocyte or macrophage infiltrates. This contrasts the other cases as well as Case 1-lung LUL, which highlights the disparate immune responses to SARS-CoV-2 even within the same patient.

We then used an unbiased tSNE clustering of all ROIs and identified two distinct clusters (Fig. 4c). Cluster 1 included the majority of the RNA-ISH positive ROIs and a smaller proportion of ISH negative ROI, while Cluster 2 included the majority of RNA-ISH negative ROI, control SARS-CoV-2 negative lung samples, and a minority of RNA-ISH positive ROI. Differential expression analysis between clusters noted high enrichment of ISGs (*ISG15*, *IRF7*, *IRF9*) in Cluster 1. Other genes overexpressed in Cluster 1 were chemokine and cytokine related genes (*CCL15*, *CCL18, TNF*, *IL11RA*, *XCR1*), the immune checkpoint protein PD-1 (*PDCD1*), and cancer-related genes (*SSX1* and *MAGEA4*). Consistent with the bulk RNA sequencing data,

17

unsupervised hierarchical clustering of ROIs using ISGs showed that SARS-CoV-2 positive

ROIs were highly enriched for IFN response (Fig 4e). This demonstrates that the IFN response

genes are preferentially expressed in regions of SARS-CoV-2 virus and not as a generalized

inflammatory response in lung. Moreover, we hypothesize that SARS-CoV-2 negative ROIs in

Cluster 1 represent resolving viral clearance and that Cluster 2 potentially represents never

infected regions of lung or unresponsive lung regions with SARS-CoV-2 virus.

To determine if these changes are driven by specific samples, we performed differential

expression of ROIs within each lung sample and identified consistent commonly expressed

genes in each lung sample (Fig. 5a). Not surprisingly, the number of differentially expressed

genes within lung samples was driven by the amount of SARS-CoV-2 heterogeneity within

samples (i.e. Case 1 and 7 had more genes differentially expressed between SARS-CoV-2

positive vs. negative ROIs). Of the genes that were differentially expressed in multiple patients,

(Fig. 5b) the majority were again related to IFN response including gene expression of ISGs

(*GBP1*, *IFITM1*, *IFI6*) and MHC Class I (*HLA-A*, *HLA-B*, *HLA-C*, *HLA-F*, *B2M*, *TAP1*). Analysis

of protein expression in these same samples (Fig. 5c) revealed elevated immune checkpoint

proteins in virus high ROIs including CTLA4 and PD-L1 in Case 1 and 7 lung samples. IDO1

protein was also elevated in these cases, which was also seen at the RNA level in both the

GeoMx DSP analysis (Fig. 5b) and in bulk RNA-seq as an IFN gamma response gene (Fig. 2b).

Similarly, PD-L1 protein was elevated in Cases 1 and 7 (Fig. 5c) with PD-L1 RNA expression

(*CD274*) elevated in Cluster 1 (Fig. 4e). IHC staining and whole slide quantification of PD-L1

and IDO1 in samples did not identify clear differences (Supplementary Fig. 6), which illustrates

the importance of analyzing ROIs to uncover intrapulmonary relationships between SARS-CoV-

2 and host response. Notably, IDO1 staining was predominantly found in endothelial cells,

which suggests a relationship between viral infection and changes in pulmonary vascular

response.

18

Finally, we attempted to dissect the intrapulmonary heterogeneity of the IFN response by looking at different classes of IFN genes that were co-expressed with each other (Fig. 5d). Genes that are secreted or associated with extracellular signaling molecules including *CXCL9*, *CXCL10*, and *IDO1* were expressed at much higher levels in SARS-CoV-2 positive ROIs compared to other genes related to MHC Class I (*HLA-A*, *HLA-B*, *HLA-C*, *HLA-F*, *B2M*) or genes related to antiviral cellular response (*IFI6*, *IFIT3*, *IFITM1*). The high levels of IDO1 identified in endothelial cells by IHC (Supplementary Fig. 6) and the known expression of *CXCL9* and *CXCL10* in endothelial cells suggests these differences may be related to local viral effects on vasculature, but other cell types including monocytes/macrophages can be the source of the expression of these genes. The spatial patterns in these IFN response genes indicate that there are differences in local host response to the virus compared to the more diffuse impact of IFN pathway activation in the lung. Altogether, there is clear intrapulmonary heterogeneity of SARS-CoV-2 infection with a non-uniform IFN response by the immune system with activation of immunoregulatory pathways (PD1/PD-L1, CTLA4, IDO1).

19

**Fig. 4 Intrapulmonary heterogeneity of SARS-CoV-2 host response.**
a, Selection of ROIs. Left) SARS-CoV-2 RNA-ISH staining was used to guide ROI selection of viral positive and viral negative regions. Right) multi-color immunofluorescence staining for CD45/red, CD68/yellow, PanCK/green and DNA/blue were used in parallel to select ROIs. Example ROIs are shown in insets.
b, Distribution of immune subsets and relationship with viral location. Rows show estimates from distinct cell types; columns show distinct tissues. Point position shows the physical location of regions within each tissue. Point size shows a cell type's estimated proportion of cells in a region. Point color denotes whether a region was classified SARS-CoV-2 positive or negative by RNA-ISH.
c, tSNE clustering of geometric ROIs highlights two primary clusters exist within the data irrespective of SARS-CoV-2 RNA-ISH status of ROI or patient viral load.
d, Differential expression analysis of clusters identified by tSNE analysis. Target genes colored by significance and association with tSNE clusters. Targets with FDR < 0.05 are shown in gray. Genes shown in red are associated with higher expression cluster labeled 'active' in panel C; genes shown in blue are associated with higher expression in the cluster labelled 'inactive'.
e, Unsupervised clustering analysis of interferon stimulated genes cluster across ROIs. Annotation by patient sample identifier and SARS-CoV-2 RNA-ISH positivity in the ROI as performed by GeoMx Digital Spatial Profiler.

21
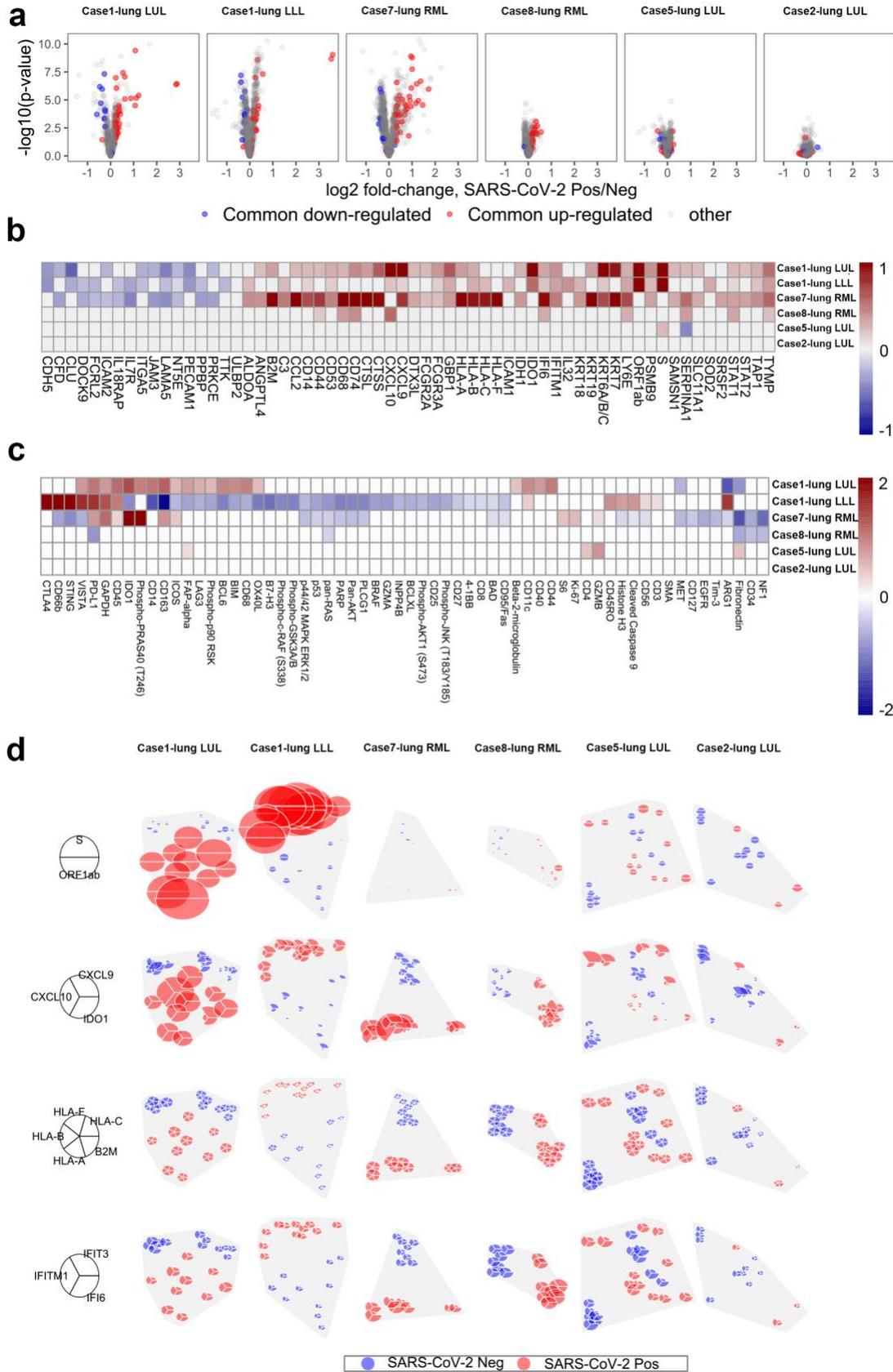
Fig. 5 Spatial Distribution of Innate Immune Response Linked with Presence of SARS-CoV-2 Virus.

a, Differential expression of all genes between SARS-CoV-2 positive/negative regions within each tissue. Horizontal position shows genes' log2 fold-change, with points farther right having higher expression in SARS-CoV-2 positive regions. Vertical position shows -log10(p-value), which increases with statistical significance. Red points show genes that were consistently up-regulated, blue points show genes that were consistently down-regulated in SARS-CoV-2 positive regions across the 6 patient tissues. Each gene has the same point color in all 6 panels.

b, Genes with consistent differential expression between SARS-CoV-2 positive/negative regions across all tissues. Only consistently up/down-regulated genes (red/blue in panel a) are shown. Grid color shows log2 fold-change, with red indicating higher expression in virus-positive regions. Results with p < 0.01 are given color. Columns are ordered by hierarchical clustering.

c, Protein differential expression between SARS-CoV-2 positive/negative regions. Only proteins with FDR < 0.05 in at least one tissue are shown. Grid color shows log2 fold-change, with red indicating higher expression in virus-positive regions. Results with p < 0.01 are given color. Columns are ordered by hierarchical clustering.

d, Spatially-resolved expression of viral and interferon signaling genes. Rows show distinct gene sets; columns show distinct tissues. Pie position shows the physical location of regions within each tissue. Wedge volume shows a gene's background-subtracted expression; within each row, all genes are scaled to have the same maximum. Wedge color denotes whether a region was classified SARS-CoV-2 positive or negative by ISH.

23

DISCUSSION

This study supports two phases of disease evolution in patients with severe COVID-19 pneumonia: 1) high viral RNA with abundant extracellular virus, and a histologic picture of exudative diffuse alveolar damage, and 2) low (or undetectable) viral RNA, a mixed histologic picture, but dominated by an organizing form of diffuse alveolar damage. The high viral cases were associated with a shorter disease duration, high expression of IFN pathway genes, and activation of wound healing and endothelial genes indicative of tissue damage and initiation of fibrosis. Although these could represent two distinct disease phenotypes, we favor a model of an early phase of the disease characterized by acute cellular injury, high viral load, and a robust IFN response followed by a late form of disease associated with tissue organization on histology and expression profiling, viral clearance, and a waning IFN response.

The IFN response is the primary early defense against viruses including SARS family of viruses. Viral detection by various pathogen recognition mechanisms stimulates the production of type I and type III IFN resulting in the expression of ISGs via the JAK-STAT signaling pathway. In preclinical models, SARS-CoV-2 viral infection of human intestinal epithelial cells elicits a robust IFN response that is efficient at controlling viral replication and *de novo* virus production[17]. The current study demonstrates a more nuanced view of the expression of ISGs and ties their expression with the presence of virus and duration of disease; notably, we were able to document the association at the levels of individual air spaces. Collectively, the data suggest the IFN response in SARS-CoV-2 correlated with clearance of the virus from the lung. While the IFN gene signature characterize the patients with high viral load, there was no clear immune or cytokine signature in patients with a low virus and in a later phase of the disease. Instead, in low viral cases we find indication of resolution of wound healing, presence of M0 and M2 macrophages, and return of pulmonary epithelial cells.

24

Our results are consistent with recent data that suggests SARS-CoV-2 appears to be responsive to IFN-I treatment *in vitro* and more sensitive than SARS-CoV[18]. Initial clinical data with IFN beta-1b, lopinavir-ritonavir, and ribavirin has shown some promise with decreased time to clearance of SARS-CoV-2 from nasopharyngeal swab testing[19]. However, the results contrast with recent efforts that show minimal amounts of IFNs in the peripheral blood of patients with severe COVID-19[5,6]. These two studies have suggested that type-I IFN deficiency in the blood could be a hallmark of severe COVID-19, although neither study evaluated pulmonary tissue. The presence of robust expression of numerous ISGs in bronchoalveolar lavage fluid from SARS-CoV-2 supports this hypothesis[20]. While the precise role of the IFN response and its ability to clear virus remains an open question, our work underscores the possibility of a robust IFN response in the majority of patients with severe COVID-19 infection and that these IFN producing cells may remain localized to the lung. The study also highlights the challenges associated with using blood as a surrogate to assess pulmonary disease in viral pneumonia, and this is further compounded by the temporal and spatial heterogeneity of the virus and corresponding immune response.

The use of the GeoMX[TM] digital spatial profiler has provided unprecedented spatial transcriptomic and proteomic analysis of the intra-pulmonary heterogeneity of SARS-CoV-2 infection. Within individual lobes, infected airspaces with significant interferon response pathway activation were juxtaposed to uninvolved lung tissue providing an opportunity to understand regional variation in lung tissue response to the virus. This intra-patient heterogeneity also extended to immune subsets, best exemplified in Case 1 in which a prominent population of dendritic cells, plasmacytoid dendritic cells, NK, and T-cells in one lobe was distinct from the more common monocyte/macrophage heavy infiltrate seen in another lobe of the same patient. Analysis of virus high ROIs across all cases showed significant interferon

25

response gene expression compared to virus low ROIs, but we note there were two outlier

genes *SSX1* and *CCL15* that were very high in virus high ROIs. *SSX1* is known mostly as a

partner of the SS18-SSX1 translocation commonly found in synovial sarcoma, and interestingly,

has been found to be upstream of *SHCBP1* expression[21], a gene involved with paramyxovirus

viral replication and suppression of the interferon response[22,23]. This suggests that *SSX1* may

be induced by SARS-CoV-2 as an adaptive response to interferon, but further mechanistic

studies will be needed to evaluate this hypothesis. *CCL15*, also known as leukotactin-1, is

highly expressed in M1 compared to M2 macrophages[24] and is a chemokine involved with

chemotaxis of neutrophils, monocytes, and lymphocytes[25]. The presence of higher M1

macrophages in SARS-CoV-2 high cases would indicate that *CCL15* is important in the immune

response to the virus. Our analysis of proteins enriched in high virus ROIs revealed enriched

expression of multiple immune checkpoint molecules including CTLA4, PD-L1, and IDO1, which

supports an immune microenvironment that is inhibitory to T-cell activation. Prior studies have

reported T cell exhaustion or increased expression of inhibitory receptors on peripheral blood T

cells of COVID-19 patients supporting these findings of T-cell suppression[7,26,27].

Determining the phase of the disease in the lungs, specifically the peak and nadir, may have

therapeutic implications. Given the clear interferon response to the virus in early infection,

immunosuppressive therapy would potentially be most effective in the decelerating viral load

phase of the disease. A recent preliminary report of dexamethasone use in COVID-19 patients

demonstrated an improvement of 28-day mortality among those who were receiving either

invasive mechanical ventilation or oxygen alone but not among those receiving no respiratory

support[28]. Notably, dexamethasone was associated with a reduction in 28-day mortality among

those with symptoms for more than 7 days but not among those with a more recent symptom

onset, findings consistent with high viral load in the early phase of the disease. Our data also

supports the likely greater benefit of antiviral therapy such as remdesivir in the early phase of

26

the disease given high viral levels associated with diffuse alveolar damage. The data also raise

the provocative hypothesis that many patients clear SARS-CoV-2 within two weeks of the onset

of the disease, largely driven by a robust IFN response. However, the small, but detectable

presence of virus RNA in low viral cases would indicate potential continued benefit of antivirals

in later stages of the disease. The presence of T-cell inhibitory molecules (CTLA4, PD-L1,

IDO1) in high virus cases also suggests that immune checkpoint inhibitors could have a role in

patients with ineffective immune response, though this is highly speculative. The RNA-ISH and

qRT-PCR assay could potentially be performed as complementary diagnostics on

bronchoalveolar lavage samples to distinguish the two phases of the disease as well as

discriminate active infection from asymptomatic carrier with another pulmonary process.

However, one notable caveat is the heterogeneity in viral load, necessitating that multiple lobes

must be sampled.

In summary, detailed molecular analysis of multiple lung lobes from patients with severe

COVID-19 infection highlights two phases in patients who succumb to the disease. While anti-

viral agents are likely to be most beneficial earlier in the disease, the timing and type of immune

modulation, activating or inhibiting, must be carefully considered given the heterogeneous

immune responses observed in these patients. Our findings highlight the importance in serially

assessing tissue pulmonary SARS-CoV-2 RNA levels and the immune response as well as

attempt to identify corresponding surrogate markers in the blood, although the heterogeneity in

the viral load and immune response across the lobes of the lung may prove a challenge.

Additional mechanistic and biomarker driven studies of SARS-CoV-2 are needed to optimize

patient selection and the timing of treatment administration to address this inherent spectrum of

COVID-19 presentation. The current work provides the foundation to evaluate a larger series of

autopsies characterizing the spatiotemporal relationship of viral load and host microenvironment

27

response, and these findings will help inform the design of current and future interventional

trials.

Data Availability Statement

All RNA-seq data has been uploaded to NCBI GEO GSE150316. All NanoString GeoMX data

will be uploaded to NCBI GEO and released before publication.

Code Availability Statement

There was no custom code or mathematical algorithm used for this work. All software for RNA-

seq and NanoString GeoMX data analysis is described in the methods and all software will be

provided if requested.

METHODS

Immunohistochemistry and RNA-ISH

Analysis of patient autopsy material was reviewed and approved by the Partners Human

Research IRB (Protocol #: 2020P001001). Autopsy consent was per clinical care as directed by

the patient or health care proxy. We evaluated hematoxylin and eosin (H&E) stained sections

from FFPE tissue from the lungs, heart, liver, intestine, bone marrow, adipose tissue and

kidney. We performed immunohistochemistry (IHC) for CD3, CD8, CD20, CD163, CD123,

IDO1, PD-L1, Napsin A, keratin and SARS-CoV N protein on an immunohistochemical platform.

RNA-ISH was performed on FFPE sections using a SARS-CoV-2 RNA specific probe on an

automated Leica BOND RX (RNAscope 2.5 LS Probe V-nCoV2019-S, #848568, and

RNAscope 2.5 LS Reagent Kit-RED, #322150; Advanced Cell Diagnostics). Slides were imaged

using a Leica Aperio CS-O slide scanning microscope at 40x magnification. Image

quantification was performed using Halo software (Indica Labs). Tissue regions of interest were

annotated by hand, excluding any folds or debris. The Multiplex IHC module was used to

28

calculate the number of positive cells per square millimeter of tissue. Areas of pulmonary

parenchyma with positive SARS-CoV-2 RNA ISH signal were annotated manually. The

percentage of ISH signal was calculated as follows: area of lung parenchyma with positive

signal/area of total lung parenchyma.

Protein Target	company	Clone	Antibody dilution	Antibody incubation	Epitope retrieval condition
CD3	Leica	LN3	Ready to use	15 minutes	ER2 for 15 minutes
CD8	Leica	4B11	Ready to use	15 minutes	ER2 for 20 minutes
CD20	Leica	L26	1:100	15 minutes	ER1 for 30 minutes
CD163	Leica	10D6	Ready to use	15 minutes	ER2 for 20 minutes
Napsin A	Leica	IP64	1:200	15 minutes	ER2 for 20 minutes
CD123	Leica	BR4MS	1:100	15 minutes	ER2 for 20 minutes
PDL1	Cell Signaling	E1L3N	1:200	15 minutes	ER2 for 20 minutes
IDO	Cell Signaling	D5J4E	1:400	30 minutes	ER2 for 20 minutes
SARS nucleocapsid	Novus Biologicals	NB100-56576	1:250	30 minutes	ER2 for 20 minutes
WS keratin	Dako	Z062201-2	1:900	15 minutes	ER2 for 20 minutes

All the IHC staining was performed on Leica Biosystem Bond III with Leica Bond Polymer
Refine Detection (Catalog number DS9800)

Molecular RNA Analysis

We performed total RNA-seq and quantitative reverse transcriptase polymerase chain reaction

(qRT-PCR). RNA extraction from FFPE slides was done using the FormaPure Total nucleic acid

extraction kit (C16675, Beckman Coulter) according to manufacturer instructions. Three 5 um

thin tissue sections from areas devoid of acute inflammation were used per sample. SARS-CoV-

2 RNA was detected in extracts from FFPE samples with qRT-PCR by following the guidelines

of the Center for Disease Control and Prevention for the qRT-PCR diagnostic panel. A total of 1

29

ng of RNA input was used per reaction. 1-step qRT PCR was performed with the GoTaq Probe

1-Step RT-qPCR kit (A6120, Promega) using the CDC-approved 2019-nCoV RUO primer-probe

kit (10006713, IDT). For Total RNA-sequencing, The Smarter Stranded Total RNA-Seq kit v2

(634413, Illumina) was used with 10 ng RNA input, according to the manufacturer instructions to

generate libraries. Dual-indexed pooled libraries were sequenced on the Illumina NextSeq 500

platform using a 150 cycles kit with paired end read mode. For RNA expression analysis, the

initial quality control of sequencing data was carried out using the tool FASTQC and alignment

of sequencing reads to the reference genome was carried out using STAR aligner, version 2.7

[29]. We used the genome annotation and GTF for SARS-CoV-2 available on NCBI. A joint

annotation was created by adding the COVID19 genome to the HG38 genome sequence and

the GTF sequence. A new index for STAR aligner was created using this new annotation. Post

alignment using this new annotation, the duplicate reads were marked using PICARD and

removed using SAMtools. The resulting BAM files were used to quantify the read counts per

gene using HTSeq-count program. The downstream analysis was carried out in the R statistical

programming language including hierarchical clustering. The DESeq2 package[30] was used for

differential expression analysis between samples. Cell type deconvolution from gene expression

was performed using CIBERSORTx[31] using the LM22 signature matrix and batch correction for

bulk sorted reference profiles. Plots were made using the heatmap.2 function in the gplots

package in R. All RNA-seq data has been uploaded to NCBI GEO GSE150316.

GeoMx DSP for protein profiling

Autopsy tissues from COVID-19 infected patents were processed following the GeoMx DSP

slide prep user manual (MAN-10087-04). Autopsy FFPE slides were baked in oven at 60°C for

at least 1 hour, and then rehydrated and blocked by Nanostring block buffer for 1 hour. CD68-

594 (Novus Bio, NBP2-34736AF647), CD45-647 (Novus Bio, NBP2-34527AF647), and PanCK-

488 (eBioscience, 53-9003-82) were added on the sections along with the Nanostring protein

cocktail for overnight incubation. The slides were washed and stained with Syto83

(ThermoFisher, S11364) on the next day. 20X fluorescent images were scanned after loading

the slides to GeoMx machine. Regions of interest (ROIs) in Alveoli were selected in both

COVID19 high and COVID19 low regions based on the COVID-19 ISH staining in the serial

section. Oligos from antibodies were cleaved and collected into 96-well plates. Then these

oligos were hybridized with NanoString barcodes overnight and read with an nCounter machine.

Digital accounts of each antibody in each ROI were generated for data analysis.

GeoMx DSP for CTA profiling

Autopsy FFPE tissues from COVID-19 infected patents were processed following the GeoMx

DSP slide prep user manual (MAN-10087-04). Autopsy slides were baked in oven at 60°C for at

least 1 hour, and then deparaffinized and hydrated by Leica Biosystems BOND RX. Proteinase

K was added prior to the incubation of incubated with RNA probe mix (CTA and COVID-19

spike-in panel). After overnight incubation, slides were washed with buffer and stained with

CD68-594 (Novus Bio, NBP2-34736AF647), CD45-647 (Novus Bio, NBP2-34527AF647), and

PanCK-488 (eBioscience, 53-9003-82) and Syto83 (ThermoFisher, S11364) for 1 hour, and

loaded to the GeoMx DSP machine to scan 20X fluorescent images. Regions of interest (ROIs)

were placed by aligning to the ROIs placed during protein profiling. Oligos were cleaved and

collected into 96-well plates. Oligos from each AOI was uniquely indexed using Illumina's i5 x i7

dual-indexing system. 4 uL of a GeoMx DSP sample was used in the PCR reaction. PCR

reactions were purified with two rounds of AMPure XP beads (Beckman Coulter) at 1.2x bead-

to-sample ratio. Libraries were paired-end sequenced (2x75) on a NextSeq550 up to 400M total

aligned reads. Fastq files were further process by DND system and raw and Q3 normalized

counts of all CTA targets in each AOI were obtained through Nanostring Azorius program.

31

Spatial Transcriptomics Analysis

Analysis of GeoMx protein data

Per manufacturer's recommendations, the data was normalized by scaling to the negative

control IgG probes, which reflect the rate at which antibodies bind to each region. The Ms IgG2a

probe was excluded from this calculation due to poor concordance with the other IgGs. 6 ROIs

were removed due to low signal. 10 proteins were excluded from analysis due to lack of above-

background signal. For each tissue and each protein, differential expression vs. SARS-CoV-2

presence/absence was evaluated with an unpaired, heteroscedastic t-test of the protein's log2-

transformed normalized data.

GeoMx RNA data normalization

Probes for each gene were screened for outliers and their raw counts collapsed to a single

estimate of counts using their geometric mean. Each ROI's data was scaled to have the same

75th percentile.

Estimation of background in GeoMx RNA data

For each data point (gene x ROI), the expected background was estimated as the geometric

mean of the negative control probes from the appropriate probe pool (CTA or COVID-19 spike-

in) within the ROI in question. These expected background values were used as an input in

mixed cell deconvolution and for background-subtraction in the plot of spatially-resolved

expression.

Deconvolution of cell proportions from GeoMx RNA data

Cell mixing proportions were estimated using the SpatialDecon R library, which performs

mixture deconvolution using constrained log-normal regression. The algorithm was run using a

32

cell profile matrix derived from the Human Cell Atlas adult lung 10X dataset and appended with a neutrophil profile derived from snRNA-seq of lung tumors[32]. The neutrophil profile was scaled to have the same 75_{th} percentile expression value as the average cell type's profile in the Human Cell Atlas lung dataset.

Differential Expression Analysis of GeoMx RNA data

Only genes that rose 2-fold above background in at least one ROI were considered. For each tissue and each gene, differential expression vs. SARS-CoV-2 presence/absence was evaluated with an unpaired, heteroscedastic t-test of the gene's log2-transformed normalized data. For analysis of expression within tissues, genes were defined as consistently up-regulated if they 1. had a log2 fold-change > 0.2 and a Benjamini-Hochberg FDR < 0.1 in at least 2 tissues, and 2. never had a log2 fold-change < 0 and a Benjamini-Hochberg FDR < 0.1 in any tissue. Genes were defined as consistently down-regulated by an equivalent rule.

For analysis across patient samples, expression was modeled using linear mixed effect models allowing for random slope and intercept terms per patient sample. P-values were estimated using Satterthwaite's method for approximation, and adjusting using the Benjamini-Hochberg FDR.

COMPETING INTERESTS

33

REFERENCES

1. Zhu, N.*, et al.* A Novel Coronavirus from Patients with Pneumonia in China, 2019. *New England Journal of Medicine* **382**, 727-733 (2020).

2. Carsana, L.*, et al.* Pulmonary post-mortem findings in a series of COVID-19 cases from northern Italy: a two-centre descriptive study. *Lancet Infect Dis* (2020).

3. Liao, M.*, et al.* Single-cell landscape of bronchoalveolar immune cells in patients with COVID-19. *Nat Med* **26**, 842-844 (2020).

4. Ong, E.Z.*, et al.* A Dynamic Immune Response Shapes COVID-19 Progression. *Cell Host Microbe* **27**, 879-882 e872 (2020).

5. Blanco-Melo, D.*, et al.* Imbalanced Host Response to SARS-CoV-2 Drives Development of COVID-19. *Cell* **181**, 1036-1045 e1039 (2020).

6. Hadjadj, J.*, et al.* Impaired type I interferon activity and inflammatory responses in severe COVID-19 patients. *Science* (2020).

7.   Schultheiss, C.*, et al.* Next-Generation Sequencing of T and B Cell Receptor Repertoires from COVID-19 Patients Showed Signatures Associated with Severity of Disease. *Immunity* (2020).

8.   Huang, C.*, et al.* Clinical features of patients infected with 2019 novel coronavirus in Wuhan, China. *Lancet* **395**, 497-506 (2020).

9.   Mehta, P.*, et al.* COVID-19: consider cytokine storm syndromes and immunosuppression. *Lancet* **395**, 1033-1034 (2020).

10.   Henderson, L.A.*, et al.* On the alert for cytokine storm: Immunopathology in COVID-19. *Arthritis Rheumatol* (2020).

11.   Chen, G.*, et al.* Clinical and immunological features of severe and moderate coronavirus disease 2019. *J Clin Invest* **130**, 2620-2629 (2020).

12.   Hoffmann, M.*, et al.* SARS-CoV-2 Cell Entry Depends on ACE2 and TMPRSS2 and Is Blocked by a Clinically Proven Protease Inhibitor. *Cell* **181**, 271-280 e278 (2020).

13.   Wang, K.*, et al.* SARS-CoV-2 invades host cells via a novel route: CD147-spike protein. *bioRxiv*, 2020.2003.2014.988345 (2020).

14.   Ziegler, C.G.K.*, et al.* SARS-CoV-2 receptor ACE2 is an interferon-stimulated gene in human airway epithelial cells and is detected in specific cell subsets across tissues. *Cell* (2020).

15.   Rooney, M.S., Shukla, S.A., Wu, C.J., Getz, G. & Hacohen, N. Molecular and genetic properties of tumors associated with local immune cytolytic activity. *Cell* **160**, 48-61 (2015).

16.   Merritt, C.R.*, et al.* Multiplex digital spatial profiling of proteins and RNA in fixed tissue. *Nat Biotechnol* **38**, 586-599 (2020).

17.   Stanifer, M.L.*, et al.* Critical Role of Type III Interferon in Controlling SARS-CoV-2 Infection in Human Intestinal Epithelial Cells. *Cell reports* **32**, 107863 (2020).

35

18. Mantlo, E., Bukreyeva, N., Maruyama, J., Paessler, S. & Huang, C. Antiviral activities of type I interferons to SARS-CoV-2 infection. *Antiviral Res* **179**, 104811 (2020).

19. Hung, I.F.-N.*, et al.* Triple combination of interferon beta-1b, lopinavir–ritonavir, and ribavirin in the treatment of patients admitted to hospital with COVID-19: an open-label, randomised, phase 2 trial. *The Lancet* **395**, 1695-1704 (2020).

20. Zhou, Z.*, et al.* Heightened Innate Immune Responses in the Respiratory Tract of COVID-19 Patients. *Cell Host Microbe* **27**, 883-890 e882 (2020).

21. Peng, C.*, et al.* Identification of SHCBP1 as a novel downstream target gene of SS18-SSX1 and its functional analysis in progression of synovial sarcoma. *Oncotarget* **7**, 66822-66834 (2016).

22. Lo, M.K., Sogaard, T.M. & Karlin, D.G. Evolution and structural organization of the C proteins of paramyxovirinae. *PLoS One* **9**, e90003 (2014).

23. Minako Ito, M.I., Makoto Takeda, Takanori Nakamura, Yusuke Yanagi, Shinji Ohno. Measles Virus Nonstructural C Protein Modulates Viral RNA Polymerase Activity by Interacting with Host Protein SHCBP1. *Journal of Virology* **87**, 9633–9642 (2013).

24. Martinez, F.O., Gordon, S., Locati, M. & Mantovani, A. Transcriptional Profiling of the Human Monocyte-to-Macrophage Differentiation and Polarization: New Molecules and Patterns of Gene Expression. *The Journal of Immunology* **177**, 7303-7311 (2006).

25. Youn, B.S.*, et al.* Molecular cloning of leukotactin-1: a novel human beta-chemokine, a chemoattractant for neutrophils, monocytes, and lymphocytes, and a potent agonist at CC chemokine receptors 1 and 3. *The Journal of Immunology* **159**, 5201-5205 (1997).

26. Mathew, D.*, et al.* Deep immune profiling of COVID-19 patients reveals distinct immunotypes with therapeutic implications. *Science* (2020).

27. Zheng, H.Y.*, et al.* Elevated exhaustion levels and reduced functional diversity of T cells in peripheral blood may predict severe progression in COVID-19 patients. *Cell Mol Immunol* **17**, 541-543 (2020).

36

28.   Dexamethasone in Hospitalized Patients with Covid-19 — Preliminary Report. *New England Journal of Medicine* (2020).

29.   Dobin, A*., et al.* STAR: ultrafast universal RNA-seq aligner. *Bioinformatics* (2012).

30.   Love, M.I., Huber, W. & Anders, S. Moderated estimation of fold change and dispersion for RNA-seq data with DESeq2. *Genome Biol* **15**, 550 (2014).

31.   Newman, A.M*., et al.* Determining cell type abundance and expression from bulk tissues with digital cytometry. *Nature Biotechnology* **37**, 773-782 (2019).

32.   Zilionis, R*., et al.* Single-Cell Transcriptomics of Human and Mouse Lung Cancers Reveals Conserved Myeloid Populations across Individuals and Species. *Immunity* **50**, 1317-1334 e1310 (2019).